Excited oxygen kinetics at electronvolt temperatures via 5-MHz RF-diplexed laser absorption spectroscopy

Nicolas Q Minesi, Anil P Nair, Miles O Richmond, Nicholas M Kuenning, Christopher C Jelloian, R. Mitchell Spearrin

To be published in Applied Optics:

Title: Excited oxygen kinetics at electronvolt temperatures via 5-MHz RF-diplexed laser absorption spectroscopy

Authors: Nicolas Minesi,Anil nair,Miles Richmond,Nicholas Kuenning,Christopher Jelloian,Mitchell Spearrin

Accepted: 16 December 22

Posted 22 December 22

DOI: https://doi.org/10.1364/AO.479155

Excited oxygen kinetics at electronvolt temperatures via 5-MHz RF-diplexed laser absorption spectroscopy

NICOLAS Q. MINESI*, ANIL P. NAIR[1], MILES O. RICHMOND[1], NICHOLAS M. KUENNING[1], CHRISTOPHER C. JELLOIAN[1], AND R. MITCHELL SPEARRIN[1]

[1] Department of Mechanical and Aerospace Engineering, University of California, Los Angeles (UCLA), CA 90095, USA
* Corresponding author: minesi@ucla.edu

Compiled December 21, 2022

A multi-MHz laser absorption sensor at 777.2 nm (12,863 cm^{-1}) is developed for simultaneous sensing of (1) O($^5S^0$) number density, (2) electron number density, and (3) translational temperature at conditions relevant to high-speed entry conditions and molecular dissociation. This sensor leverages a bias tee circuit with a DFB diode laser and an optimization of the laser current modulation waveform to enable temporal resolution of sub-microsecond kinetic at electronvolt temperatures. In shock-heated O_2, the precision of the temperature measurement is tested at 5 MHz and is found to be within $\pm$ 5% from 6,000 to 12,000 K at pressures from 0.1 to 1 atm. The present sensor is also demonstrated in a CO:Ar mixture, in parallel with a diagnostic for CO rovibrational temperature, providing an additional validation across 7500–9700 K during molecular dissociation. A demonstration of the electron number density measurement near 11,000 K is performed and compared to a simplified model of ionization. Finally, as an illustration of the utility of this high-speed diagnostic, the measurement of the heavy particle excitation rate of O($^5S^0$) is extended beyond the temperatures available in the literature and is found to be well represented by $k(^3P \rightarrow {}^5S^0) = 2.7 \times 10^{-14} T^{0.5} \exp(-1.428 \times 10^4 / T)$ $cm^3 \cdot s^{-1}$ from 5,400 to 12,200 K.

http://dx.doi.org/10.1364/ao.XX.XXXXXX

1. INTRODUCTION

During atmospheric entry, low-pressure gases are shock-heated by high-velocity vehicles which can reach speeds of 5–10 km/s, for Mars and Venus entry, and up to 7–14 km/s, for Moon- or Mars-return entry [1, 2]. In these environments, the molecular species reach electronvolt temperatures (1 eV = 11,605 K) leading to rapid dissociation and ionization. Atomic oxygen can be formed by the dissociation of O_2, present in the terrestrial atmosphere, and CO_2, present in the Venusian and Martian atmospheres. In the visible spectrum of air, the formation of electronically excited atoms lead to intense radiation that can account for a non-negligible contribution to the plasma radiating power at $T > 8000$ K [3–5]. In conditions relevant for lunar-return entry (7–9 km/s), the radiation in the 700–1020 nm range is dominated by atomic radiation and represents approximately 30% of the radiative flux during peak heating [6]. Therefore, it is crucial to understand the formation and depletion of these states during entry.

The simulation of the electronic excitation of shock-heated gases can be conducted through multi-temperature models [1, 2] or using state-to-state models [7, 8]. In a multi-temperature model, the population distribution of the atomic oxygen electronic states, shown in Fig. 1, can be calculated based on the electronic temperature. In a state-to-state simulation, electronic states can be modeled as pseudo species, at the cost of increasing the computation time. A collisional-radiative state-to-state model of the Fire II flight experiment (Earth entry above 10 km/s) demonstrated that in selected points of the trajectory, the O electronic states lying above 5 eV departed from the Boltzmann and the Saha equilibrium [8]. Thus, simulations more accurate than multi-temperature models must be performed to correctly describe the electronic excitation. For that purpose, accurate state-to-state rates of formation/depletion are needed.

The formation and radiation of atomic oxygen is typically studied by optical emission spectroscopy (OES) [5] and resonance absorption spectroscopy [9]. The transition of atomic oxygen at 777.2 nm (777.4 nm in vacuum) was studied in an inductively coupled plasma torch at steady-state by laser absorption spectroscopy (LAS) [10]. Several recent works in shock

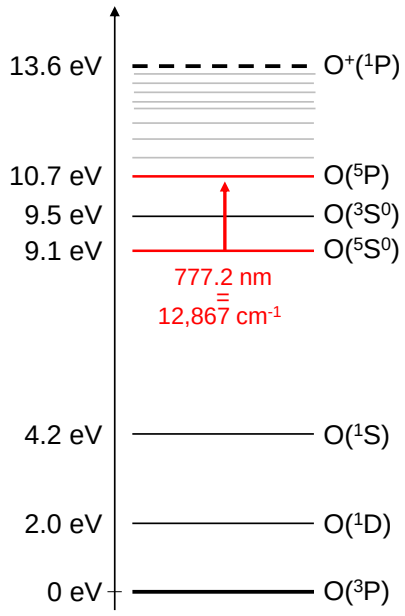

Fig. 1. Simplified distribution of O electronic energy levels with J degeneracy omitted.

tubes have contributed to an increased understanding of excited oxygen kinetics. In the 5400–8000 K temperature range, Nations et al. [11] measured $O(^5S_2^0)$ and $O(^3S_1^0)$ number density using the transitions at 777.2 and 844.6 nm, see Fig. 1. These relatively low temperatures of electronic excitation required an off-axis optical cavity to amplify the absorption signal. These data lead to the determination of the $O(^5S_2^0)$ and $O(^3S_1^0)$ excitation rate by Ar collisions [12]. At higher temperatures, this work was pursued by Li et al. who extended one of these rates up to 10,000 K [13] and measured the shock-induced ionization via the Stark shift effect of oxygen transitions [14]. The electron number density, which can also be measured via emission techniques [15], is of primary importance because the electron collisions dominate the electronic excitation of atoms at high ionization rates. Based on laser absorption measurements, Li et al. [16] demonstrated that the population of electronically excited O evolves according to three phases: (i) excitation by heavy impact, (ii) depletion by cold electrons, and (iii) excitation by electron impact. The time resolution in [11, 13, 14] was 10–20 µs (rate of 50–100 kHz). Near 0.1 atm and 10,000 K, the duration of phase (i) is near 10 µs, which is equal to the time resolution of the aforementioned measurements. The experimental investigation of the population/depletion process of an O electronic state during this phase would be enhanced by employing faster measurement rates. Therefore, a faster sensor with sub-µs resolution is needed for examining excited oxygen kinetics at higher pressures and temperatures, reflective of higher speed entry.

In previous works, our group has presented techniques to improve the scan depth, signal-to-noise ratio (SNR), and time resolution of LAS measurements using customized opto-electronics and optimized modulation waveforms. In [17, 18], a bias tee circuit was employed to diplex DC current generated from a laser controller with an RF modulation signal, effectively bypassing the current-controller bandwidth limitation (around 200 kHz). This DFB laser modulation scheme increased previous limits in scan depth or measurement speed by one order of magnitude, sufficient to capture multiple rovibrational transitions of CO and CO_2 at several MHz [18–20]. Further scan-depth improvement was achieved more recently by scanning DFB lasers below the lasing threshold and employing a squared current waveform modulation [21]. This type of modulation, also demonstrated in [22], increased the temperature variations experienced by the laser chip within one scan period and multiplied the spectral scan depth by more than two compared to sine wave modulation. Moreover, most of the spectrum is scanned while the laser is at its maximum output power, which increases the measurement SNR.

In the present work, such advanced laser modulation techniques are employed to spectrally-resolve the $^5P_3 \leftarrow {}^5S_2^0$ transition of O at 777.2 nm at multi-MHz rates in order to resolve excited oxygen kinetics at electronvolt temperatures. The sensor simultaneously measures the $O(^5S_2^0)$ number density, the translational temperature, and the electron number density with a measurement integration time of tens of nanoseconds. In Section 2, the theoretical foundations of this work and the data processing methods are discussed. In Section 3, the experimental setup is described. Finally, in Section 4, the performance of the sensor is validated. We demonstrate the relevance of this sensor by resolving the $O(^5S_2^0)$ number density with at 5 MHz and determine the rate of $O(^5S_2^0)$ formation by heavy collisions.

2. METHODS

A. Laser absorption spectroscopy principles

The methods and principles of laser absorption spectroscopy are extensively discussed in [23]. The absorbance α_i of a single line can be calculated using the incident and transmitted light intensities I_0 and I_t, respectively:

$$\alpha(\nu) = -\ln\left(\frac{I_t}{I_0}\right)_\nu \quad \textbf{(1)}$$

For a uniform gas, the Beer-Lambert law relates the spectrally-integrated absorbance area, A [cm^{-1}], of a single spectral feature, i, to the species number density, n [cm^{-3}], the optical pathlength, L [cm], and the linestrength, $S(T)$ [cm^{-1}/(molec·cm^{-2})], at the gas temperature, T [K]:

$$\int_\nu \alpha(\nu)d\nu = A = nLS(T) \quad \textbf{(2)}$$

The linestrength of the $^5P_3 \leftarrow {}^5S_2^0$ transition can be calculated using Eq. 3 where $hc/k = 1.44$ cm·K, $c = 3\times10^{-10}$ cm/s, $f_{12} = 0.468$ is the oscillator strength of the $^5P_3 \leftarrow {}^5S_2^0$ transition [24], and $\nu_0 = 12,863$ cm^{-1} is the transition wavenumber.

$$S(T) = (8.83\times10^{-13})\frac{f_{12}}{c}\left(1-\exp\left(-hc\nu_0/kT\right)\right) \quad \textbf{(3)}$$

B. Broadening and shift mechanisms

In this work, the transition lineshape is assumed to be a Voigt, a convolution of the Gaussian and Lorentzian lineshapes arising due to different broadening mechanisms. These mechanisms were theoretically derived by Griem in several textbooks [25, 26] and later summarized [5, 23, 27].

The Gaussian broadening and the corresponding full width at half maximum (FWHM), $\Delta\nu_D$ [cm^{-1}] in Eq. 4, originates solely from the Doppler broadening and is a function of the line center

Table 1. Stark parameters calculated for the 777 nm triplet of atomic oxygen [App. IV, 25].

T_e [K]	w [nm]	d [nm]	α
5,000	2.28×10^{-2}	144×10^{-3}	0.16
10,000	3.15×10^{-2}	1.43×10^{-3}	0.12
20,000	4.47×10^{-2}	1.30×10^{-3}	0.10
40,000	6.03×10^{-2}	1.08×10^{-3}	0.08

frequency ν_0 = 12,863 cm^{-1} and the molar mass of the particle M_O = 16 g·mol^{-1}.

$$\Delta\nu_D = \nu_0(7.16 \times 10^{-7})\sqrt{\frac{T}{M_O}} \quad (4)$$

The Lorentzian FWHM is the sum of several broadening mechanisms. The natural line broadening originates from the finite lifetime in vacuum of the initial and final states of the transition. The natural FWHM, usually negligible, can be calculated using Eq. 5, where $A_{\text{up, k}}$ and $A_{\text{down, k}}$ are the Einstein A coefficients of all downwards transitions from the upper and lower state and c is the speed of light.

$$\Delta\nu_{\text{nat}}[\text{cm}^{-1}] = \frac{1}{2\pi c}\left(\sum_k A_{\text{up, k}} + \sum_k A_{\text{low, k}}\right) \quad (5)$$

Resonant broadening is due to the dipole interaction of the transition upper and lower levels to other like-atoms. Non-straightforward formulas for evaluating this broadening source are available [5, 25–27] and a simplified expression for the oxygen triplet at 777 nm was derived in [28], see Eq. 6.

$$\Delta\nu_{\text{res}}[\text{nm}] = \beta(T)\frac{n_O}{2.7 \times 10^{19}\ \text{cm}^{-3}} \quad (6)$$

The combination of the coefficient β(10,000 K) = 9×10^{-6} nm, tabulated in [Table A4, 28], and the number density of atomic oxygen, n_O, induce an extremely low self-broadening effect, which is therefore negligible in the present work.

Van der Waals broadening, or non-resonant pressure broadening, can be calculated using Eq. 7, where P [atm] is the pressure, X_B the mole fraction of the collision partner B, and $\gamma_{O\leftarrow B}$ [cm^{-1}/atm] the broadening coefficient of species B on O.

$$\Delta\nu_{\text{van der Waals}}[\text{cm}^{-1}] = P\sum_B X_B 2\gamma_{O\leftarrow B} \quad (7)$$

The γ coefficient is typically modeled by the power law of Eq. 8 where $\gamma(T_0)$ [cm^{-1}·atm^{-1}] is the broadening coefficient at the reference temperature T_0 and N is the temperature exponent.

$$\gamma_{O\leftarrow B} = \gamma(T_0)\left(\frac{T_0}{T}\right)^N \quad (8)$$

For T_0 = 298 K, The measured coefficients of Eq. 8 for argon are N =0.6985 and $2\gamma(T_0)$ = 0.4615 cm^{-1}/atm [11], which is in line with the theory of Griem predicting N = 0.7 [25, 26]. In some cases of this work, the gas will be composed at up to 2% of atomic oxygen, O, and 1% of atomic carbon, C, whose van der Waals coefficients are not available experimentally. According to the Griem theory, the van der Waals broadening scales with $\alpha^{0.4}/\mu^{0.3}$ where α is the perturber polarizability and μ the perturber-radiator reduced mass [26, 27]. The atoms polarizabilities are α_{Ar} = 11.08, α_C = 11.3, α_O = 5.3 in atomic units [29]. The reduced masses are μ_{Ar} = 11.4, μ_C = 6.8, and μ_O = 8 in g/mol. Therefore, the van der Waals coefficients of O and C are expected to be 0.8 and 1.1 times that of Ar, respectively. Given that O and C are only present as traces in these experiments (< 1%), their presence has a negligible influence on the van der Waals broadening and we will employ Eq. 8 with the argon coefficient determined experimentally by Nations et al. [11].

Table 2. FWHM in cm^{-1} of the atomic O transition at 12,863 cm^{-1} (777.2 nm) in a bath gas of argon where T [K] is the gas temperature, P [atm] the pressure, n_e [cm^{-3}] the electron number density, and ω [nm] the Stark coefficient. Ion effects on Stark broadening are neglected in this table only.

$\Delta\nu_{\text{Doppler}}$	$\Delta\nu_{\text{nat}}$	$\Delta\nu_{\text{res}}$	$\Delta\nu_{\text{van der Waals}}$	$\Delta\nu_{\text{Stark}}$
$2.3 \times 10^{-3}\sqrt{T}$	1.9	< 0.001	$24.7P/T^{0.6985}$	$33\omega n_e/10^{16}$

The van der Waals shift is 1/3 of the van der Waals broadening [26]. Given that the pressure change is minimal in the reflected region of the shock tube experiments, the van der Waals shift is assumed to be constant in the entire analysis of this paper [14].

Finally, the Stark effect arises due to the interaction of the upper and lower states of the transition with electrons and ions [25–27]. The Stark broadening, $\Delta\nu_{\text{Stark}}$, and the Stark shift, $\delta\nu_{\text{Stark}}$, can be calculated following Eqs. 9 & 10 where n_e [cm^{-3}] is the electron number density and T_e [K] is the electron temperature.

$$\Delta\lambda_{\text{Stark}}[\text{nm}] = 2\left[1 + 1.75 f_{\text{ion}}(T_e, n_e)\right]\omega\frac{n_e}{10^{16}\ \text{cm}^{-3}} \quad (9)$$

$$\delta\lambda_{\text{Stark}}[\text{nm}] = \left[d \pm 2 f_{\text{ion}}(T_e, n_e)\omega\right]\frac{n_e}{10^{16}\ \text{cm}^{-3}} \quad (10)$$

With the present case, the sign in Eq. 10 is a "+" [14, 26]. The quasi-static field generated by the ions is responsible for the factor f_{ion}.

$$f_{\text{ion}}(T_e, n_e) = 10^{-4} n_e^{0.25}\alpha\left(1 - 0.068 n_e^{\frac{1}{6}} T_e^{-0.5}\right) \quad (11)$$

The d, w, and α coefficients were initially tabulated in 1964 by Griem [26] but Griem corrected them in 1974 [App. IV, 25] by about 10% (reproduced in Table 2). The ion correction term, f_{ion}, is comparatively small and, in consequences, the Stark broadening and shift are approximately linear with the electron number density and the ion correction term is small. At T_e = 10,000 K and n_e = 10^{16} cm^{-3}, conditions representative of the present work, the ion correction induces a +3% contribution to the broadening and a +6% to the shift. Nevertheless, we employed the full expression in this work. At the present wavelength, the conversion from "nm" to "cm^{-1}" can be obtained by multiplying Eqs. 9 & 10 by 16.55 cm^{-1}/nm (using $\delta\nu = -\delta\lambda/\lambda^2$ and $\Delta\nu = \Delta\lambda/\lambda^2$).

A summary of the broadening formula is given in Table 2. In Fig. 2, the aforementioned broadening FWHM are calculated for the 777.2 nm transition in a 1% O_2 at chemical equilibrium. The Doppler broadening is clearly dominant across the temperatures and pressures studied in this work. The van der Waals broadening decreases with temperature due to the $T^{-0.7}$ term in Eq. 7. Above 8000 K, a significant fraction of the neutral particles are ionized. Thus, the van der Waals broadening decreases faster than $T^{-0.7}$ and the relative importance of Stark broadening quickly increases.

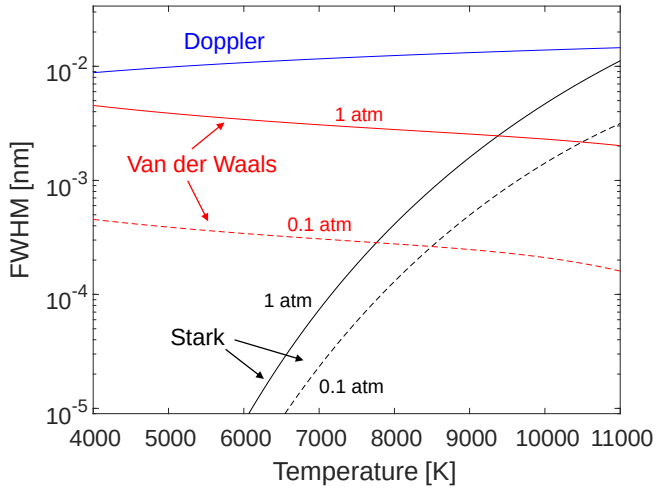

Fig. 2. Calculated broadenings in O_2:Ar = 1:99 at equilibrium.

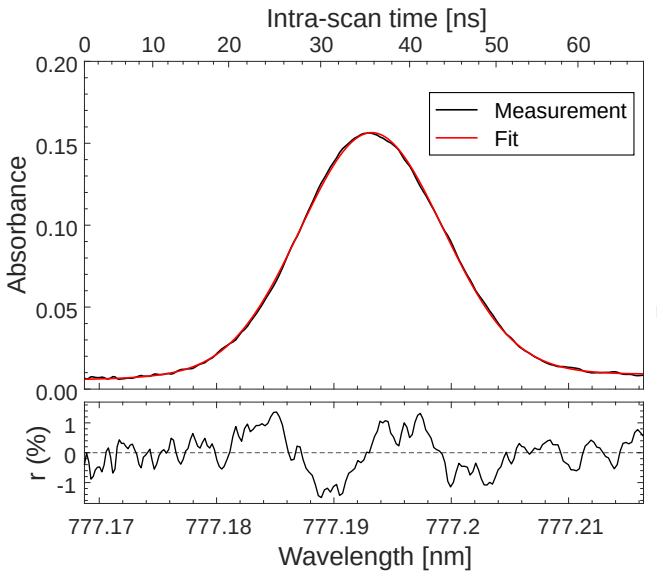

Fig. 3. Typical fit of an experimental spectrum scanned at 5 MHz. The residual is normalized with the peak absorbance.

C. Fitting procedure

In the present work, the background intensity is determined from an average of the laser scans across 10s of microseconds ahead of the incident shock. The absorbance spectrum for each measurement scan is calculated according to Eq. 1. A Voigt profile, approximated using the polynomial expression of McLean [30], is fitted to the experimental spectrum by floating the area, the line center, and the Doppler width. For temperatures below 8000 K, the impact of Stark broadening is negligible. Therefore the Lorentzian width is assumed to be equal to the collisional broadening (see Eq. 7). For temperatures higher than 8000 K, the Lorentzian width is floated to account for the Stark broadening contribution. A linear baseline is also fitted to the experimental spectrum to account for the plasma emission during the experiment. When possible, the baseline is assumed to be a constant function to lower the measurement noise. An example of a fitted measurement is shown in Fig. 3.

3. EXPERIMENTAL SETUP

Shock tubes can generate high temperatures across a range of pressures with high certainty in gas composition and thermodynamic state. They are therefore well-suited for developing and validating optical diagnostics, among other applications. In this study, the UCLA high-enthalpy shock tube (HEST) [31, 32], presented in Fig. 4, is used to generate temperature and pressure conditions across 6000–12,000 K at 0.1–1 atm. Incident shock waves at speeds of 1.7–2.5 km/s are typically generated in gas mixtures of O_2:Ar and CO:Ar by bursting a polycarbonate, aluminium, and copper diaphragms. Helium is used as a driver gas. Before each shock, the driven section is turbo-vacuumed to less than 500 µTorr for at least two hours. The shock-wave time-of-arrival is measured by five piezoelectric sensors (Dynasen, CA-1135) located in the driven section. LAS measurements are conducted 2 cm from the shock-tube end wall through two 0.5-degree wedged sapphire windows. The reflected shock conditions are calculated using normal shock relations, assuming vibrational equilibrium conditions ahead of the reflected shock [33]. The region 2 chemistry has a negligible effect on region 5, due to the low concentration of O_2 in Ar.

A stainless-steel mixing tank is used to prepare the gas mixtures manometrically. The tank is vacuumed down to less than 20 mTorr before preparing the mixtures. The purity of CO, O_2, and Ar gases is certified above or equal to 99.99% by Airgas. The combined pressure and pure gas uncertainties result in a relative mixture composition uncertainty below 0.2%. Thus, the uncertainty of the reference mixture is assumed to be negligible.

The optical setup is schematically presented in Fig. 4. A distributed feedback laser (DFB, Nanoplus) is regulated in mean current and temperature using a laser controller (Arroyo 6305). A fixed (DC) current is sent to the laser via the controller, while a high-frequency modulation (1 to 5 MHz) is added to this DC component via a bias-tee circuit [18]. In this work, we modulate the laser with a trapezoidal waveform which presents a larger spectral scan-depth and SNR compared to sine or sawtooth modulations [21]. As shown in Fig. 4, a ramp is applied on the increasing side of the trapezoidal-wave modulation. The slope of this ramp is an effective way to control the speed of the spectrum scan (or chirp rate). The present ramp is chosen to ensure that the temporal frequency content of the scanned spectral features is below the limiting bandwidth of the detection system (200 MHz) [21]. For experiments including CO sensing, this optical setup is supplemented with the optical setup of [34], including a quantum cascade laser (QCL, Alpes Lasers) regulated in temperature with a laser controller (Arroyo 6310-QCL). In a similar fashion to the O* sensor, a bias-tee and a trapezoidal waveform are also employed to modulate the QCL laser at 1 MHz.

As observed in prior works [35–37], the fast chirping of DFB lasers increases the laser linewidth, $\Delta\nu_{\text{chirp}}$ [cm^{-1}], which can be calculated using Eq.12 where $d\nu/dt$ [$\text{cm}^{-1}/\mu\text{s}$] is the chirp rate, $c = 3 \times 10^4$ cm/µs the speed of light, and $\beta < 1$ [36].

$$\Delta\nu_{\text{chirp}} = \sqrt{\beta \frac{1}{c} \frac{d\nu}{dt}} \tag{12}$$

Assuming $\beta = 1$ and with a maximal scanning speed of 1 $\text{cm}^{-1}/\mu\text{s}$ for CO and 8 $\text{cm}^{-1}/\mu\text{s}$ for O*, the artificial broadening due to the chirping is at most $\Delta\nu_{\text{chirp}} < 0.015$ cm^{-1}, which is negligible compared to physical broadening mechanisms described in Section 2.B.

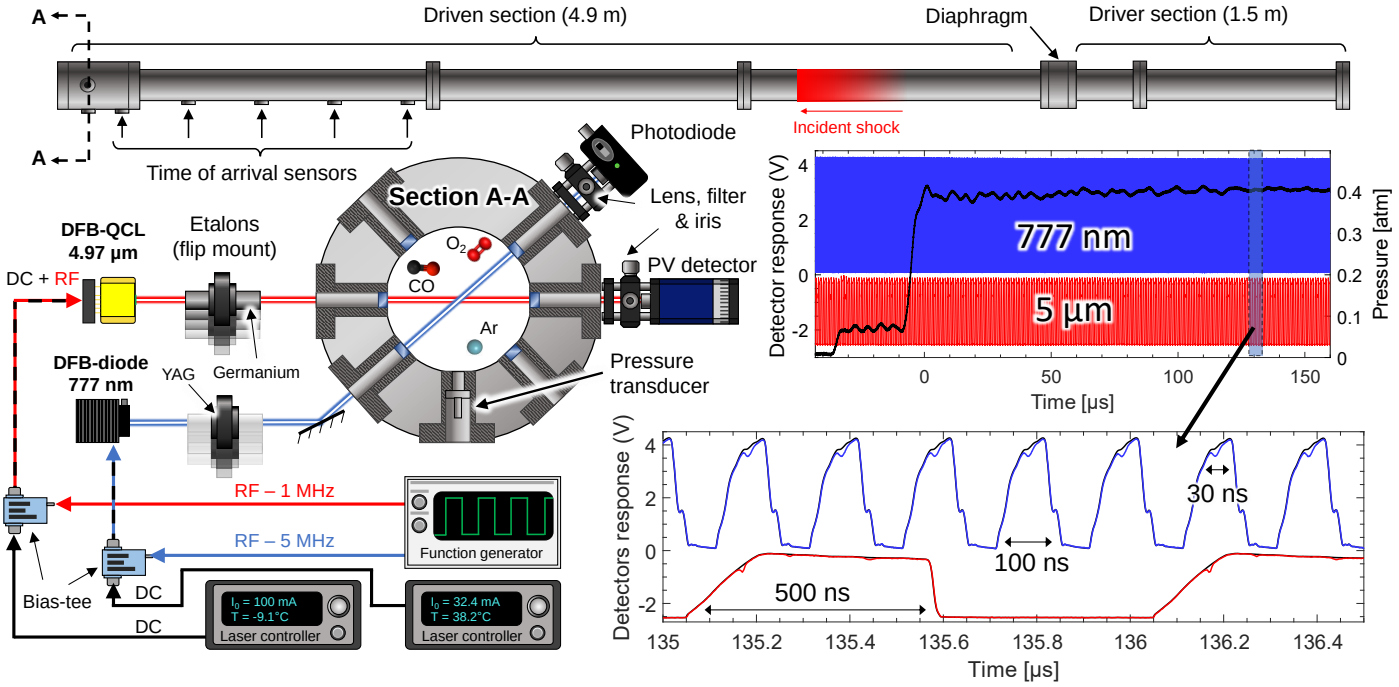

Fig. 4. (Left) Opto-electronic setup mounted on the UCLA shock tube. The measurements are performed at cross-section A-A near the end wall of the shock tube. (Right) Raw pressure and light-intensity measurements. In the inset, the time-resolved measurements of O* and CO (in blue and red) are compared with the averaged background (in black). Offset in the raw voltages are added for clarity.

Detection of the 777.2-nm optical signals is focused with a 15-mm lens on a photodiode (Thorlabs, PDA102, 150 MHz bandwidth) whose output is sent to a Tektronix oscilloscope (MSO44 model, bandwidth 200 MHz) sampling the data on a 12-bit scale at 3.125 GS/s or higher. The broadband shock-induced emission is blocked by a narrow bandpass filter (Thorlabs). For CO, the detection is performed on a photovoltaic (PV) detector (Vigo, PVI-4TE-5-1x1, 10 Hz–205 MHz bandwidth) through an AR-coated calcium-fluoride lens (20-mm focal length) and a narrow band-pass filter near 5 µm [34]. The raw data acquired on the oscilloscope are presented in Fig. 4 and synchronized with the pressure measurement performed by a high-speed pressure transducer (Kistler, 601B1). An inset of Fig. 4 gives a comparison between the average background laser intensity recorded before the incident shock arrival, I_0, and the time-resolved transmitted laser intensity measured by the detector, I_t. The background, or baseline, laser intensity also incorporates all sources of voltage in the oscilloscope such as detector dark noise and the unfiltered plasma emission. The methods for conversion of I_0 and I_t into physical measurements were presented in the previous section. Validation and demonstration of sensor capabilities are presented in the following sections.

4. SENSOR DEMONSTRATION

A. Temperature measurement

In this subsection, the temperature measurement performed via the Doppler broadening is compared to the ideal conditions generated by the shock tube. An example of the O(^{5}S^0) number density and temperature measured at 5 MHz in the reflected region is shown in Fig. 5. The reference temperature is calculated using Eq. 13, where T_{shock} is either the incident or reflected shock temperature (T_2 or T_5) and $\Delta T_{\text{diss}}^{(O_2)}$ is the temperature drop due to the oxygen dissociation.

$$T_{\text{ref}} = T_{\text{shock}} - \Delta T_{\text{diss}}^{(O_2)} \quad \textbf{(13)}$$

The level of O_2 dissociation is calculated 10 µs after the shock using the rate of dissociation in Eq. 14 [38].

$$k_d(T)[\text{cm}^3/(\text{mol}\cdot\text{s})] = 2.87\times10^{18}T^{-1}\exp(-58580/T) \quad \textbf{(14)}$$

The level of dissociation is typically higher than 85% 10 µs after a reflected shock (and near 65% in two incident shock tests). A linear increase of the pressure is observed behind the reflected shock and induces an isentropic compression, which is included in the reference temperature calculation.

For a set of conditions from 6,000 to 12,000 K, the measured temperature is compared to T_{ref} in Fig. 6. For two shock conditions, the 777.2-nm transition is above the sensor detection limit (near $\sim10^8$ cm^{-3}) in the incident shock region and is used for temperature validation. The reflected region of these two particular experiments is not used. The measured temperature is taken across 10 µs (50 samples at 5 MHz) right before the reflected shock. Outside these two particular measurements in the incident region, the measured temperature is averaged from 10 to 20 µs after the reflected shock. This period corresponds to a low peak absorbance at 7000–9000 K because O(^{5}S^0) is still being formed, but coincides with the peak of O(^{5}S^0) number density at 10,000–12,000 K, see Fig. 5. The reported y-uncertainty in Fig. 6 is the standard deviation of the temperature measurement across 10 µs, and is close to the single-point measurement uncertainty. The x-uncertainty on the reference temperature is estimated from the predicted post-shock temperature uncertainty, mainly driven by the shock speed uncertainty, see [App B, 34]

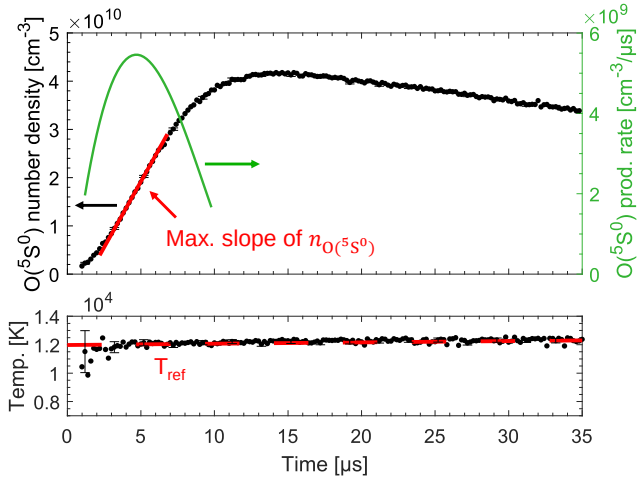

Fig. 5. O_2:Ar = 1:99 shock-heated at T_5 = 12,199 K and p_5 = 0.23 atm. *Top:* Rate determination using the fitted rate production of $O(^5S^0)$. The slope of the $O(^5S^0)$ number density increase, in red, is for illustration only. *Bottom:* Measured temperature compared to T_5 accounting for a slight pressure rise.

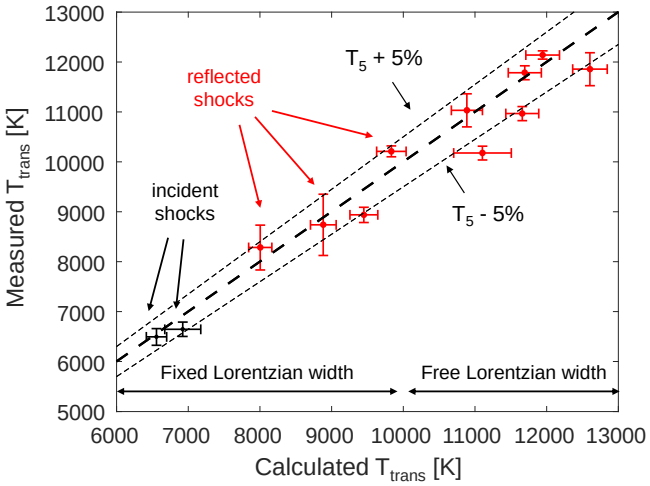

Fig. 6. Measured temperature compared to shock-heated temperature. The temperature drop due to the O_2 dissociation is included in the reference temperature.

B. Electron number density measurement

As described in Section 2.B, the presence of electrons induce a broadening and a shift of the oxygen line. Thus, the electron number density could theoretically be measured using the FWHM of the transition. However, as shown in Fig. 2, the Stark broadening will be convoluted with the van der Waals and Doppler broadenings. The contribution of the Stark effect will be difficult to evaluate given that Doppler broadening will be dominant up to 11,000 K. On the other hand, line shifting arises only due to the van der Waals and the Stark effects. In a shock tube environment, the pressure is abruptly increased by the incident and reflected shocks but remains stable otherwise. In this study, the steepest pressure increase reported in the reflected region is 0.07 atm per 100 μs. This pressure increase leads to a shift of less than 10^{-4} cm^{-1} per 100 μs, which would corresponds to an increase of the electron number density of 4×10^{13} cm^{-3} if it was interpreted as a Stark shift. This value is rather low compared to the measurement noise, around 3×10^{14} cm^{-3}. The van der Waals shift is therefore assumed constant and the variations of the line position is solely due to the increase or decrease of the ionization fraction.

The increase of the electron number density, n_e, is shown in Fig. 7 after a reflected shock. The electron number density is assumed to start at zero right after the reflected shock. A nearly linear increase of n_e at a rate close to 10^{15} cm^{-3} per 100 μs is observed. The 5-MHz sampling being higher than the typical timescale of increase, we average the electron number density to an apparent 1-MHz sampling. This procedure increases the SNR of the measurement, while remaining as fast as the measurement performed by Cruden [15] who used emission spectroscopy at ionization rates ∼10 times higher.

The measurements of Fig. 7 are compared to a simplified model inspired by [16]. In our kinetic simulations, the production and depletion of the electrons is due heavy and electron impact collisions:

$$\mathrm{Ar} + \mathrm{Ar} \longleftrightarrow \mathrm{Ar} + \mathrm{e^-} + \mathrm{Ar^+} \qquad \textbf{(R1)}$$

$$\mathrm{e^-} + \mathrm{Ar} \longleftrightarrow \mathrm{e^-} + \mathrm{e^-} + \mathrm{Ar^+} \qquad \textbf{(R2)}$$

Using the forward and reverse rates optimized in [16] and assuming a constant (free) electron temperature, T_e = 9200 K, we find reasonable agreement with our measurements. At first, electron production is dominated by (R1). Then, the change of slope in the simulated n_e is due to the start of the electron impact ionization, (R2). It should be emphasized that this model is only employed to compare order of magnitudes and give a reference to our measurement. A more rigorous model, such as [16], should include other minor channels of ionization and the electron energy equation to account for the evolution of T_e. Model results from a 200-K change in T_e are also shown in Fig. 7.

C. Dynamic comparison with CO laser absorption spectroscopy

In this subsection, the measurements performed with the 777.2-nm transitions are compared to those performed with high-temperature LAS CO sensor developed recently [34]. Thus, for this section only, we report measurements in CO:Ar mixtures, whereas all the results displayed in other sections were obtained in O_2:Ar mixtures.

This paragraph quickly summarizes the details behind the fitting of CO transitions, which are fully developed in our previous work [34]. Four CO transitions – R(8,24), R(10,115), P(4,7), and P(1,25) – are scanned at 1 MHz across 2010.6–2011.6 cm^{-1}. The CO linestrengths and CO partition function are calculated using the HITEMP 2019 database [39, 40]. Using the areas of these lines, a Boltzmann population fit is performed and provides CO number density and temperature. The fitting procedure is performed assuming equilibrium of the rotational and vibrational temperatures, which is typically the case in the conditions explored here. From 7000 to 9000 K, the uncertainties are calculated according to the methods in [34]. The 1-MHz sampling being extremely fast compared to the timescale of temperature and CO mole fraction evolution, the measurements were time averaged to 100 kHz. This procedure improved the experimental spectrum signal-to-noise ratio, which in turns reduced the uncertainty. Thus, the uncertainty is typically within 3–5% for number density and 1–3% for temperature.

The temperatures measured via both techniques are dis-

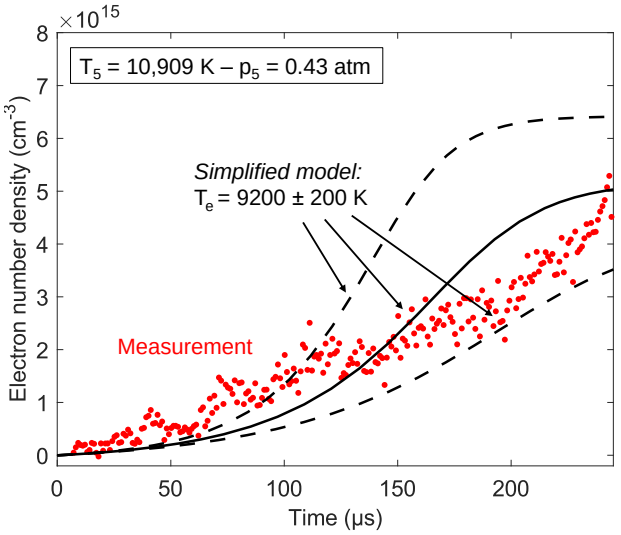

Fig. 7. Measured electron number density based on Stark shift of the 777.2-nm transition at T_5 = 10,909 K and p_5 = 0.43 atm. These measurements are compared to a simplified model described in Section 4.B

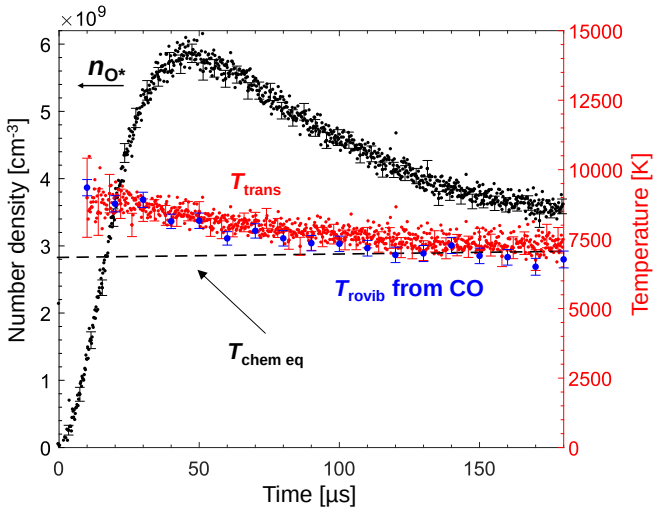

Fig. 8. Mixture of CO:Ar = 6:94 shock-heated at T_5 = 9755 K and p_5 = 0.34 atm. Comparison of the temperature measured using O*, in red, and the CO lines, in blue. The chemical equilibrium temperature is calculated accounting for the CO dissociation and the slight pressure increase in the reflected region.

played in Fig. 8. The low number density of $O(^5S^0)$ induces a slight scatter in the translational temperature measurement, as anticipated by the error bar. The rovibrational temperature measured with the CO sensor shows smaller error bars due to the 100 kHz resampling. The agreement between the rovibrational and translational temperature is excellent. After 100 μs, the measurements reach the equilibrium temperature calculated at fixed enthalpy and accounting for the slight pressure rise behind the reflected shock. The $O(^5S^0)$ number density, notated n_{O^*}, reaches a maximum at t = 50 μs and then slowly decays. This decay can be due to the decrease of temperature, from T_5 = 9755 K to ∼7500 K or the multistage behavior described in the next section.

D. O* kinetic rate determination

In [13], a three-phase behavior is reported in the $O(^5S^0)$ population time history. First, O_2 is assumed to be thermally dissociated into the atomic O ground state, $O(^3P)$. $O(^5S^0)$ is primarily formed by heavy particle impact of Ar on $O(^3P)$:

$$\mathrm{Ar} + \mathrm{O}(^3\mathrm{P}) \longrightarrow \mathrm{Ar} + \mathrm{O}(^5\mathrm{S}^0) \qquad \textbf{(R3)}$$

This phase, where the $O(^5S^0)$ number density *increases*, takes 1–10 μs, see Fig. 5. Then, as the ionization fraction increases, a de-excitation process occur, where electrons at a relatively low temperature sink the electronic energy of O. The reaction (R4,r) is arbitrarily defined as the reverse direction.

$$\mathrm{e}^- + \mathrm{O}(^5\mathrm{S}^0) \longrightarrow \mathrm{e}^- + \mathrm{O}(^3\mathrm{P}) \qquad \textbf{(R4,r)}$$

This second phase, where the $O(^5S^0)$ number density *decreases*, takes 10–100 μs, see Fig. 5. Once the electron temperature is high enough, the forward direction of the reaction starts to dominate and the $O(^5S^0)$ population increases again.

$$\mathrm{e}^- + \mathrm{O}(^3\mathrm{P}) \longrightarrow \mathrm{e}^- + \mathrm{O}(^5\mathrm{S}^0) \qquad \textbf{(R4,f)}$$

This third and last phase is not visible in Fig. 5.

Past experimental and numerical work [11–14, 16] examined this multistage behavior based on measurements at 10s of kHz. In this subsection, we emphasize how the sub-μs capabilities of this present sensor complement these previous works, especially in the study of (R3). As demonstrated in Fig. 5 and 8, the measurements at 5 MHz completely resolve the increasing phase of the $O(^5S^0)$ number density. The $O(^5S^0)$ population, notated n_{O^*}, can be calculated using Eq. 15 accounting for (R3), (R4,r), and (R4,f), where n_M is the number density of species M in its ground state and k_i is the reaction rate of (R3), (R4,r), and (R4,f).

$$\frac{dn_{O^*}}{dt} = k_1(T) n_{\mathrm{Ar}} n_{\mathrm{O}} + k_{2,f}(T_e) n_e n_{\mathrm{O}} - k_{2,r}(T_e) n_e n_{O^*} \qquad \textbf{(15)}$$

In Eq. 15, the reaction rate $k_1(T)$ involving two heavy colliders is a function of the translational temperature, T, whereas the reaction rates $k_{2,f}(T_e)$ and $k_{2,r}(T_e)$ involving one electron are a functions of the electron temperature, T_e. For a shock-heated mixture at $T \sim$ 10,000 K and $p \sim$ 1 atm, the electron number density and temperature start very low. Thus, the ratio of the first and second terms is $k_1 n_{\mathrm{Ar}} / k_{2,f} n_e \sim 10$ and the ratio of the first and third terms is $k_1 n_{\mathrm{Ar}} n_{\mathrm{O}} / k_{2,r} n_{\mathrm{Ar}} n_{O^*} \sim 10$. For these estimations, we use the electron number density measurement in Section 4.B, $n_e \sim 10^{15}$ cm^{-3}. The O excitation by Ar impact is $k_1 \sim 10^{-18}$ cm^3/s at 10,000 K and the electron impact rate is evaluated at 8000 K, $k_{2,f} \sim 10^{-15}$ cm^3/s, because the electron temperature typically takes several ms to equilibrate to the translational temperature [13]. Similarly, the reverse reaction rate is estimated at 8000 K and gives $k_{2,r} \sim 10^{-8}$ cm^3/s [13]. A more detailed sensitivity analysis was performed at similar conditions by Li et al. [13] who obtained the same conclusions at the early test times. As a result, the rate of (R3) can be measured using:

$$k_1(T) \approx \frac{dn_{O^*}}{dt} \frac{1}{n_{\mathrm{Ar}} n_{\mathrm{O}}} \qquad \textbf{(16)}$$

The derivative in Eq. 16 is calculated by fitting the n_{O^*} time history with a polynomial. The maximum of this polynomial derivative, shown in Fig. 5, corresponds to the inflection point

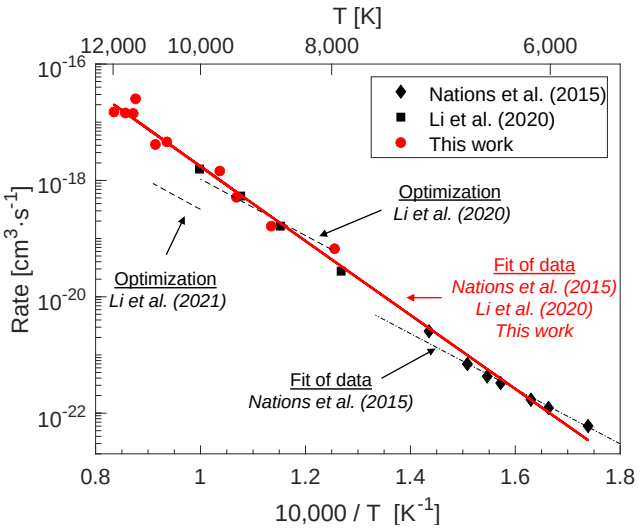

Fig. 9. Rate of O($^5S^0$) excitation by heavy collisions measured in the literature, in black, and the present work, in red.

of the O($^5S^0$) population and corresponds to the instant when (R3) begins to compete with other reactions. The ground state population of atomic O is calculated using the rate in Eq. 14. Our measurements are shown in Fig. 9, where the temperature of each measurement is calculated accounting for the slight cooling due to O_2 dissociation at the n_{O^*} derivative peak, see Eq. 13.

Our kinetic rate measurements were performed over a temperature range of 8,000–12,200 K and compared to the rates reported across several studies [12, 13, 16]. Notably, our dataset uniquely examines the near-electronvolt temperature domain due to the ability to resolve micro-second formation timescales. At lower temperature, Nations et al. [12] and Li et al. (2020) [13] adjusted the rate of (R3) by combining time resolved experiments at 10s of kHz with state-to-state simulations. The agreement in value and trend between the previous and present results (black and red data points, respectively) in the overlapping temperature range suggests consistency in our techniques to measure $k_1(T)$. In [12, 13, 16], several rates were determined following an Arrhenius form, $k(T) = AT^b \exp(-E_i/T)$, where A [cm^3/s] is the pre-exponential factor, b the temperature exponent, and E_i [K] the activation energy. All the formation rates are consistent with the corresponding datasets, but the trend over the entire temperature domain exhibits a lack of agreement with any one rate expression. This is explained by the functional form of the rate employed for the fitting in previous study, guided by Drawin's formula, where $E_{i,\text{Drawin}} = 1.061 \times 10^5$ K is the energy difference between the two levels of interest and $b_{\text{Drawin}} = 0.5$ [41]. This formulation is correct if the activation energy of (R3) is actually equal to the energy level difference and if the cross-section of Ar–O collision has the functional form proposed in [41], which is an ideal case. In Fig. 9, a new Arrhenius fit is performed using the aggregate datasets of Nations et al. [12], Li et al. [13], and this work across 5,400–12,200 K. Using a least squares regression method, the pre-exponential factor and the activation energy were adjusted, which provided the following rate:

$$k_1(T) = 2.7 \times 10^{-14} T^{0.5} \exp(-1.428 \times 10^4 / T) \quad \textbf{(17)}$$

The fitted activation energy is 34% higher than the energy separation between the electronic levels, rendering superior consistency across all temperatures. This adjustment in activation energy may be viewed as an empirical solution, given that, in other works, the reaction rate of heavy-particle impact can be modeled using other formulations than the Arrhenius law derived from the ideal Drawin's model [42, 43]. Additionally, we note that the activation energy is not strictly constrained to the separation of electronic levels.

5. UNCERTAINTY

In this section, we assess the uncertainties associated with the measurement of translational temperature, excited oxygen number density, and electron number density,

A. Temperature and number density

The analysis in this subsection follows the work presented in [18, 34] based on Taylor series expansions [44]. In this work, the translational temperature is determined from the Doppler broadening, Eq. 4. Thus, the temperature uncertainty is twice that of the Doppler broadening measurement:

$$\frac{\delta\nu_T}{\nu_T} = 2\frac{\delta\nu_D}{\nu_D} \quad \textbf{(18)}$$

It can be shown that the relative broadening uncertainty scales with the relative area uncertainty [45]. In the present work, the broadening is dominated by a Gaussian (Doppler) component and this principle can be written:

$$\frac{\delta\nu_D}{\nu_D} \approx \frac{\delta A}{A} = \frac{1}{\text{SNR}} \frac{\exp(\alpha_i^{\text{pk}})}{\alpha_i^{\text{pk}}} \quad \textbf{(19)}$$

The area uncertainty was demonstrated to be a function the measurement SNR and the peak absorbance, α_{pk}, which gives the right-hand side expression in Eq. 19 [34].

The number density uncertainty can be obtained after differentiating Eq. 2.

$$\frac{dn}{n} = \frac{dS}{S} + \frac{dA}{A} \quad \textbf{(20)}$$

The term dS/S is calculated by differentiating Eq. 3 which is related to the oscillator strength uncertainty, δf_{12}, and the derivative of S(T), $\partial S/\partial T$. Assuming the variables are independent of one another and that the errors in the measured variables are independent of one another [44], we obtain:

$$\frac{\delta n}{n} = \sqrt{\left(\frac{\delta f_{12}}{f_{12}}\right)^2_{\text{bias}} + \left(\frac{\partial S}{\partial T}\delta T\right)^2 + \left(\frac{1}{\text{SNR}}\frac{\exp(\alpha_i^{\text{pk}})}{\alpha_i^{\text{pk}}}\right)^2} \quad \textbf{(21)}$$

We used $\delta f_{12}/f_{12} = 3\%$ [24] which is a bias error when to the other terms of Eq. 21 are random errors. Note that only the random errors are reported on the figures.

B. Electron number density

To our knowledge, the Stark *shift* coefficient of the oxygen triplet at 777 nm calculated by Griem [25] have not been validated in controlled experiments [46, 47]. An experimental study confirmed that the Stark *width* of the present oxygen transition led to similar results to the well-known Stark broadening of H_α and H_β [48]. In general, the measured Stark coefficients of other oxygen lines are within a factor 0.61–1.29 times the calculated ones for the widths, and within a factor 0.48–1.17 for the shifts [46, 47]. For instance, the Stark parameters of several

atomic O lines were measured by Miller et al. [49] and found to be within 8–25% for the width and 15–40% for the shift compared to those calculated in 1964 by Griem [26]. As stated later by Griem in 1974 [pp. 196, 25], the "*average deviation*" between his calculation and experimental references is within 10–15%, but one should not rule out individual discrepancies as much as a factor 2. In a recent study [50], the Stark coefficients of the oxygen transition at 777 nm were calculated and compared to the results of Griem [25]. The width coefficients calculated in both references agree within 10%. However, the shift coefficient of [50] was found to be several times smaller than that calculated by Griem. Until further experimental validation or precise calculations, we estimate that the electron number density measured through this technique could suffer a bias within a factor of 0.5–2. Compared to these values, the bias induced by a potential under/overestimation of van der Waals shift is minimal.

6. CONCLUSIONS

In this work, a high-speed laser absorption sensor was developed to spectrally resolve the excited oxygen line at 777.2 nm (12,863 cm^{-1}) at up to 5-MHz measurement rates to examine non-equilibrium kinetics relevant to planetary entry at temperatures in excess of 1 electronvolt. A trapezoidal current modulation waveform was fed to the laser via a bias-tee circuit which allowed a measurement rate of 5 MHz with an integration time of approximately 40 nanoseconds. This represents a new limit in measurement rate for atomic oxygen. We demonstrate that multiple properties can be retrieved from this single laser measurement, with variable performance. (1) The translation temperature measurement, derived from the Doppler broadening, is shown to match the ideal shock conditions within ±5%. An additional demonstration of the dynamic response of this sensor is performed during CO dissociation, using CO rovibrational temperature as a reference, with excellent agreement. (2) The electron number density of the plasma, measured from the Stark shift, is found to be close to a simplified model of ionization. (3) The O($^5S^0$) number density, obtained from the line area, follows the phases of formation/depletion described in the literature [13]. At 5 MHz, this sensor could reveal the fast population phase spanning a few µs after the mixture was shock heated. This speed allowed direct measurement of the rate of O($^5S^0$) formation by heavy impact (by argon) up to 12,000 K. Based on our measurement and the literature data, an Arrhenius rate is proposed across 5400–12,200 K. Using a single laser, these three measurements at 5 MHz could shed a new light on high-temperature chemistry and radiation at high-speed entry conditions.

7. BACKMATTER

Funding. Content in the funding section will be generated entirely from details submitted to Prism. Authors may add placeholder text in the manuscript to assess length, but any text added to this section in the manuscript will be replaced during production and will display official funder names along with any grant numbers provided. If additional details about a funder are required, they may be added to the Acknowledgments, even if this duplicates information in the funding section. See the example below in Acknowledgements.

Acknowledgments. This work was sponsored by NASA's Space Technology Research Grants Program via an Early Career Faculty award 80NSSC21K0066. Supplementary support was provided by a NASA Space Technology Research Fellowship 80NSSC18K1158 (C. Jelloian).

Disclosures. The authors declare no conflicts of interest.

Data availability. Data underlying the results presented in this paper are not publicly available at this time but may be obtained from the authors upon reasonable request.

REFERENCES

1. C. Park, "Review of chemical-kinetic problems of future NASA missions. I - Earth entries," J. Thermophys. Heat Transf. **7**, 385–398 (1993).
2. C. Park, J. T. Howe, R. L. Jaffe, and G. V. Candler, "Review of chemical-kinetic problems of future NASA missions, II: Mars entries," J. Thermophys. Heat Transf. **8**, 9–23 (1994).
3. S. Chauveau, C. Deron, M. Y. Perrin, P. Rivière, and A. Soufiani, "Radiative transfer in LTE air plasmas for temperatures up to 15,000 K," J. Quant. Spectrosc. Radiat. Transf. **77**, 113–130 (2003).
4. J.-M. Lamet, Y. Babou, P. Rivière, M.-Y. Perrin, and A. Soufiani, "Radiative transfer in gases under thermal and chemical nonequilibrium conditions: Application to earth atmospheric re-entry," J. Quant. Spectrosc. Radiat. Transf. **109**, 235–244 (2008).
5. C. O. Laux, T. G. Spence, C. H. Kruger, and R. N. Zare, "Optical diagnostics of atmospheric pressure air plasmas," Plasma Sources Sci. Technol. **12**, 125–138 (2003).
6. C. Johnston, "A Comparison of EAST Shock-Tube Radiation Measurements with a New Air Radiation Model," in *46th AIAA Aerospace Sciences Meeting and Exhibit,* (American Institute of Aeronautics and Astronautics, Reston, Virigina, 2008), January, pp. 1–22.
7. A. Bultel, B. G. Chéron, A. Bourdon, O. Motapon, and I. F. Schneider, "Collisional-radiative model in air for earth re-entry problems," Phys. Plasmas **13**, 043502 (2006).
8. M. Panesi, T. Magin, A. Bourdon, A. Bultel, and O. Chazot, "Fire II flight experiment analysis by means of a collisional-radiative model," J. Thermophys. Heat Transf. **23**, 236–248 (2009).
9. H. J. Mick, M. Burmeister, and P. Roth, "Atomic resonance absorption spectroscopy measurements on high-temperature CO dissociation kinetics," AIAA J. **31**, 671–676 (1993).
10. D. Baer, H. Chang, and R. Hanson, "Semiconductor laser absorption diagnostics of atomic oxygen in an atmospheric-pressure plasma," J. Quant. Spectrosc. Radiat. Transf. **50**, 621–633 (1993).
11. M. Nations, S. Wang, C. S. Goldenstein, K. Sun, D. F. Davidson, J. B. Jeffries, and R. K. Hanson, "Shock-tube measurements of excited oxygen atoms using cavity-enhanced absorption spectroscopy," Appl. Opt. **54**, 8766 (2015).
12. M. Nations, S. Wang, C. S. Goldenstein, D. F. Davidson, and R. K. Hanson, "Kinetics of Excited Oxygen Formation in Shock-Heated O 2 –Ar Mixtures," The J. Phys. Chem. A **120**, 8234–8243 (2016).
13. Y. Li, S. Wang, C. L. Strand, and R. K. Hanson, "Two-temperature Collisional-radiative Modeling of Partially Ionized O 2 –Ar Mixtures over 8000–10,000 K Behind Reflected Shock Waves," The J. Phys. Chem. A **124**, 3687–3697 (2020).
14. Y. Li, S. Wang, C. L. Strand, and R. K. Hanson, "Development of a Stark shift measurement technique using excited-state oxygen atoms to determine electron number density in shock heated O 2 /Ar above 10 000 K," Plasma Sources Sci. Technol. **30**, 025007 (2021).
15. B. A. Cruden, "Electron Density Measurement in Reentry Shocks for Lunar Return," J. Thermophys. Heat Transf. **26**, 222–230 (2012).
16. Y. Li, Y. Wang, D. F. Davidson, and R. K. Hanson, "Collisional excitation kinetics for O(3s S o 5) and O(3p P3 5) states using laser absorption spectroscopy in shock-heated weakly ionized O2 -Ar mixture," Phys. Rev. E **103**, 1–15 (2021).
17. A. P. Nair, C. Jelloian, D. S. Morrow, F. A. Bendana, D. I. Pineda, and R. M. Spearrin, "MHz mid-infrared laser absorption sensor for carbon monoxide and temperature behind detonation waves," in *AIAA Scitech 2020 Forum,* (American Institute of Aeronautics and Astronautics, Reston, Virginia, 2020).
18. A. Nair, D. Lee, D. Pineda, J. Kriesel, W. Hargus, J. Bennewitz, S. Danczyk, and R. Spearrin, "MHz laser absorption spectroscopy via diplexed RF modulation for pressure, temperature, and species in rotating detonation rocket flows," Appl. Phys. B **126**, 138 (2020).

19. M. D. Ruesch, J. J. Gilvey, C. S. Goldenstein, K. A. Daniel, C. R. Downing, K. P. Lynch, and J. L. Wagner, "Mid-Infrared Laser-Absorption-Spectroscopy Measurements of Temperature, Pressure, and NO X2 Π1/2 at 500 kHz in Shock-Heated Air," AIAA Sci. Technol. Forum Expo. AIAA SciTech Forum 2022 pp. 1–12 (2022).
20. C. C. Jelloian, F. A. Bendana, C. Wei, R. M. Spearrin, and M. E. Macdonald, "Nonequilibrium Vibrational, Rotational, and Translational Thermometry via Megahertz Laser Absorption of CO," J. Thermophys. Heat Transf. **36**, 266–275 (2022).
21. A. P. Nair, N. Q. Minesi, C. Jelloian, N. M. Kuenning, and R. M. Spearrin, "Extended tuning of distributed-feedback lasers in a bias-tee circuit via waveform optimization for MHz-rate absorption spectroscopy," Meas. Sci. Technol. **33**, 105104 (2022).
22. C. C. Jelloian, N. Q. Minesi, and R. M. Spearrin, "High-speed mid-infrared laser absorption spectroscopy of CO$$_2$$ for shock-induced thermal non-equilibrium studies of planetary entry," Appl. Phys. B **128**, 216 (2022).
23. R. Hanson, R. Spearrin, and C. Goldenstein, *Spectroscopy and Optical Diagnostics for Gases* (Springer International Publishing, 2016).
24. Wiese W L, F. J. R, and Deters T M, "Atomic Transition. Probabilities of Carbon, Nitrogen, and Oxygen — A Critical Data Compilation," J. Phys. Chem. Ref. Data p. 1 (1996).
25. H. R. Griem, *Spectral Line Broadening by Plasmas* (ACADEMIC PRESS, INC., New York, 1974).
26. H. R. Griem, *Plasma spectroscopy* (McGraw-Hill Book Company, New York, 1964).
27. S. Djurovi'c and N. Konjevi'c, "On the use of non-hydrogenic spectral lines for low electron density and high pressure plasma diagnostics," Plasma Sources Sci. Technol. **18**, 1–8 (2009).
28. N. Minesi, S. Stepanyan, P. Mariotto, G. D. Stancu, and C. O. Laux, "Fully ionized nanosecond discharges in air: the thermal spark," Plasma Sources Sci. Technol. **29**, 85003 (2020).
29. P. Schwerdtfeger and J. K. Nagle, "2018 Table of static dipole polarizabilities of the neutral elements in the periodic table," Mol. Phys. **117**, 1200–1225 (2019).
30. A. McLean, C. Mitchell, and D. Swanston, "Implementation of an efficient analytical approximation to the Voigt function for photoemission lineshape analysis," J. Electron Spectrosc. Relat. Phenom. **69**, 125–132 (1994).
31. F. A. Bendana, D. D. Lee, R. M. Spearrin, S. A. Schumaker, and S. A. Danczyk, "Infrared laser absorption thermometry and CO sensing in high-pressure rocket combustion flows from 25 to 105 bar," in *AIAA Scitech 2019 Forum,* (American Institute of Aeronautics and Astronautics, 2019), January.
32. F. A. Bendana, "Shock tube kinetics and laser absorption diagnostics for liquid- and hybrid- propellant rocket combustion analysis," Ph.D. thesis, University of California, Los Angeles (2020).
33. M. F. Campbell, K. G. Owen, D. F. Davidson, and R. K. Hanson, "Dependence of Calculated Postshock Thermodynamic Variables on Vibrational Equilibrium and Input Uncertainty," J. Thermophys. Heat Transf. **31**, 586–608 (2017).
34. N. Q. Minesi, M. O. Richmond, C. C. Jelloian, N. M. Kuenning, A. P. Nair, and R. M. Spearrin, "Multi-line Boltzmann regression for near-electronvolt temperature and CO sensing via MHz-rate infrared laser absorption spectroscopy," Appl. Phys. B **128**, 214 (2022).
35. A. A. Kosterev, F. K. Tittel, C. Gmachl, F. Capasso, D. L. Sivco, J. N. Baillargeon, A. L. Hutchinson, and A. Y. Cho, "Trace-gas detection in ambient air with a thermoelectrically cooled, pulsed quantum-cascade distributed feedback laser," Appl. Opt. **39**, 6866 (2000).
36. M. T. McCulloch, E. L. Normand, N. Langford, G. Duxbury, and D. A. Newnham, "Highly sensitive detection of trace gases using the time-resolved frequency downchirp from pulsed quantum-cascade lasers," J. Opt. Soc. Am. B **20**, 1761 (2003).
37. A. Farooq, A. B. Alquaity, M. Raza, E. F. Nasir, S. Yao, and W. Ren, "Laser sensors for energy systems and process industries: Perspectives and directions," Prog. Energy Combust. Sci. **91**, 100997 (2022).
38. K. L. Wray, "Shock-tube study of the coupling of the O2-Ar rates of dissociation and vibrational relaxation," The J. Chem. Phys. **37**, 1254–1263 (1962).
39. R. R. Gamache, B. Vispoel, M. Rey, A. Nikitin, V. Tyuterev, O. Egorov, I. E. Gordon, and V. Boudon, "Total internal partition sums for the HITRAN2020 database," J. Quant. Spectrosc. Radiat. Transf. **271**, 107713 (2021).
40. L. Rothman, I. Gordon, R. Barber, H. Dothe, R. Gamache, A. Goldman, V. Perevalov, S. Tashkun, and J. Tennyson, "HITEMP, the High-Temperature Molecular Spectroscopic Database," J. Quant. Spectrosc. Radiat. Transf. **111**, 2139–2150 (2010).
41. H. Drawin and F. Emard, "Atom-atom excitation and ionization in shock waves of the noble gases," Phys. Lett. A **43**, 333–335 (1973).
42. A. Lemal, C. M. Jacobs, M.-Y. Perrin, C. O. Laux, P. Tran, and E. Raynaud, "Prediction of Nonequilibrium Air Plasma Radiation Behind a Shock Wave," J. Thermophys. Heat Transf. **30**, 197–210 (2016).
43. S. Surzhikov, "Electronic Excitation in Air and in Carbon Dioxide Gas," RTO-EN-AVT-162 VKI lecture series **1** (2008).
44. H. W. Coleman and W. G. Steele, *Experimentation, Validation, and Uncertainty Analysis for Engineers* (John Wiley & Sons, Inc., Hoboken, NJ, USA, 2009), 3rd ed.
45. A. P. Nair, N. Q. Minesi, N. M. Kuenning, A. R. Keller, and R. Mitchell Spearrin, "Optical pressure sensing at MHz rates via collisional line broadening of carbon monoxide: uncertainty quantification in reacting flows," (submitted) .
46. N. Konjević and W. L. Wiese, "Experimental Stark widths and shifts for spectral lines of neutral and ionized atoms," J. Phys. Chem. Ref. Data **19**, 1307–1385 (1990).
47. N. Konjević, A. Lesage, J. R. Fuhr, and W. L. Wiese, "Experimental Stark Widths and Shifts for Spectral Lines of Neutral and Ionized Atoms (A Critical Review of Selected Data for the Period 1989 Through 2000)," J. Phys. Chem. Ref. Data **31**, 819–927 (2002).
48. F. P. Sainct, K. Urabe, E. Pannier, D. A. Lacoste, and C. O. Laux, "Electron number density measurements in nanosecond repetitively pulsed discharges in water vapor at atmospheric pressure," Plasma Sources Sci. Technol. **29**, 025017 (2020).
49. M. H. Miller and R. D. Bengtson, "Measured Stark Widths and Shifts for Neutral Atomic Lines," Phys. Rev. A **1**, 983–990 (1970).
50. E. Stambulchik, E. Kroupp, Y. Maron, and V. Malka, "On the Stark Effect of the O I 777-nm Triplet in Plasma and Laser Fields," Atoms **8**, 84 (2020).